Supplementary information for

DFT Reveals Why Mo Substitution Enables Multi-Electron Redox in Wadsley–Roth $Mo_xW_{1-x}Nb_{12}O_{33}$

Luke D. Salzer,[†,a] Cami Christensen,[†,a] Claire Y. Gervais,[a] Alexander G. Squires,[b] Alexis G. Manche,[b] Danielle R. Lustig,[a] Amy L. Prieto,[a] James R. Neilson,[a] David O. Scanlon,[b] Justin B. Sambur[,a]*

[a]Department of Chemistry, Colorado State University, Fort Collins, CO 80523, USA

[b]School of Chemistry, University of Birmingham, Edgbaston, B15 2TT

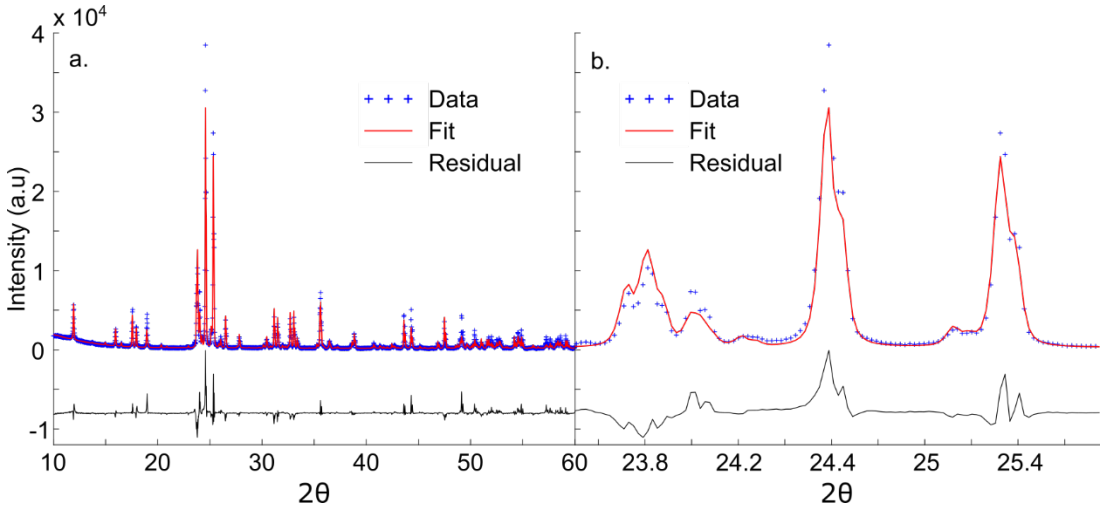

Figure S1. (a) Rietveld refinement of the slowly synthesized $Nb_{12}WO_{33}$ using the C2/m space group (R_{wp} of 20.452). (b) Zoomed-in view of the data in panel (a). The original lattice parameters for the model were 22.370Å, 3.825Å, 17.87Å, and 123.6° for a, b, c, and β respectively. The refined lattice parameters were 22.303Å, 3.826Å, 17.746Å, and 123.346° for a, b, c, and β respectively.

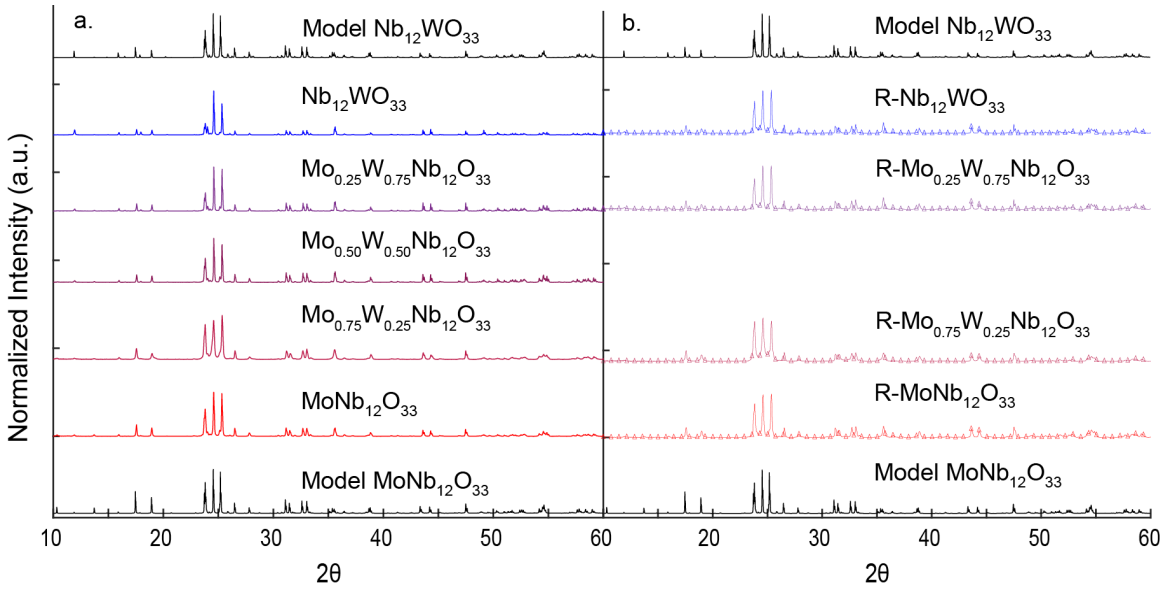

Figure S2. Comparison of simulated and experimental diffraction patterns for (a) $Mo_xW_{1-x}Nb_{12}O_{33}$ and (b) R-$Mo_xW_{1-x}Nb_{12}O_{33}$.

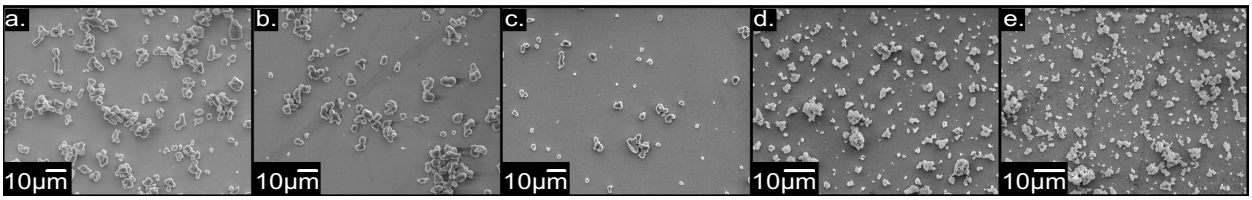

Figure S3. SEM images of (a) $Nb_{12}WO_{33}$, (b) $Mo_{0.25}W_{0.75}Nb_{12}O_{33}$, (c) $Mo_{0.5}W_{0.5}Nb_{12}O_{33}$, (d) $Mo_{0.75}W_{0.25}Nb_{12}O_{33}$, and (e) $MoNb_{12}WO_{33}$.

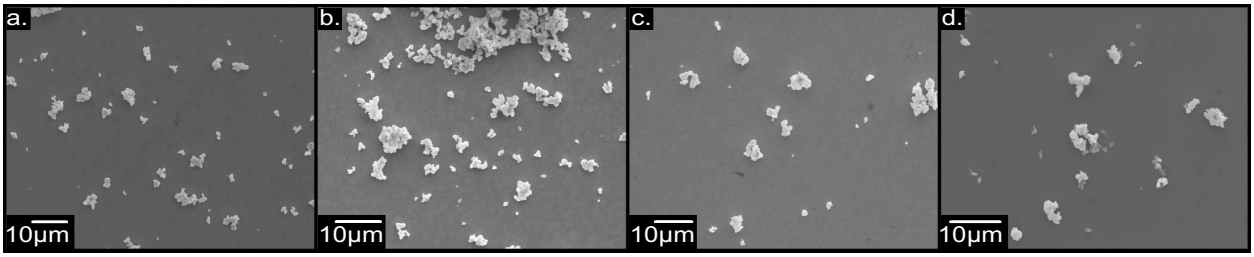

Figure S4. SEM images of (a) R-$Nb_{12}WO_{33}$, (b) R-$Mo_{0.25}W_{0.75}Nb_{12}O_{33}$, (c) R-$Mo_{0.75}W_{0.25}Nb_{12}O_{33}$, and (d) R-$MoNb_{12}WO_{33}$

Table S1. Major and minor particle lengths for $Mo_xNb_{12}W_{1-x}O_{33}$.

	$Nb_{12}WO_{33}$	$Mo_{0.25}W_{0.75}Nb_{12}O_{33}$	$Mo_{0.5}W_{0.5}Nb_{12}O_{33}$	$Mo_{0.75}W_{0.25}Nb_{12}O_{33}$	$MoNb_{12}WO_{33}$
Major Axis (μm)	3.99 ±1.4 (N=106)	3.61±1.2 (N =93)	3.23±1.1 (N =92)	1.03±0.29 (N =101)	1.02±0.35 (N =100)
Minor Axis (μm)	2.61±0.68 (N =106)	2.68±0.77 (N =93)	2.35±0.72 (N =92)	0.77±0.22 (N =101)	0.78±0.29 (N =100)

Table S2. Major and minor particle lengths for R-$Mo_xNb_{12}W_{1-x}O_{33}$.

	R-$Nb_{12}WO_{33}$	R-$Mo_{0.25}W_{0.75}Nb_{12}O_{33}$	R-$Mo_{0.75}W_{0.25}Nb_{12}O_{33}$	R-$MoNb_{12}WO_{33}$
Major Axis (μm)	1.54 ± 0.52 ($N = 71$)	1.35 ± 0.44 ($N = 76$)	1.20 ± 0.38 ($N = 42$)	1.13 ± 0.30 ($N = 24$)
Minor Axis (μm)	0.993 ± 0.30 ($N = 71$)	0.940 ± 0.83 ($N = 76$)	0.855 ± 0.27 ($N = 71$)	0.711 ± 0.21 ($N = 24$)

Table S3. Raman mode assignments using phonopy (C2/m; C2h); A_g/B_g are Raman-active (parallel vs crossed).

Spectral window (cm^{-1})	**Dominant motion (A_g/B_g)**	**Intensity**	**Trend with Mo/W and site**	**Rationale for appearance/disappearance**
200–350	Lattice modes: rigid-block tilts, interblock shears (A_g/B_g)	Moderate	Small shifts with mass/force constants; intensity modestly geometry-dependent.	Raman tensor elements are small; geometry and polarization can suppress B_g; convolution/overlap may hide weak lines.
300–500	Framework bends (O–M–O; M = Nb/Mo/W) and tilt-coupled motions (A_g/B_g)	Low	Edge/Corner add extra bending features; Tet keeps a cleaner envelope.	Local octahedral substitutions perturb connectivity → activate/boost otherwise weak bends; Tet has fewer localized bends → fewer narrow lines.

~500–600	Localized framework features tied to Edge/Corner octahedra (B_g-enhanced)	High	Edge/Corner produce new narrow bands; weak/absent for Tet.	Edge/interior octahedra rotate $\partial\alpha/\partial Q$ toward xy/yz → B_g gains; in parallel (A_g-favored) these bands can appear weak or vanish.
~620–680	Collective bends of shear-plane octahedra (A_g/B_g)	High	Tet retains a bifurcated/shouldered band; Edge/Corner shift intensity and sharpen subfeatures.	Mode mixing with nearby stretches varies with site; redistribution of oscillator strength can erase a shoulder or create an extra peak.
700–820	Nb–O–Nb stretches from block edge→interior (A_g/B_g)	Moderate	Edge/Corner concentrate intensity into the mid-frequency manifold; Tet slightly cleaner.	Edge-like Nb–O–Nb motifs are more numerous with Edge/Corner → stronger mid-frequency activity; Tet shares intensity with the high-frequency partner band.
800–900	Block-center Nb–O–Nb stretch that pairs with the tetrahedral band (predominantly A_g)	Moderate	Present and well separated for Tet; Edge/Corner reduce spacing and bleed intensity downward.	In Tet, limited mixing preserves a distinct A_g partner peak; Edge/Corner increase coupling, so intensity is borrowed away, narrowing the high-frequency gap.
900–1060	Tetrahedral M–O symmetric stretch (predominantly A_g)	High	Tet: strong, isolated highest-frequency feature; W lies tens of cm^{-1} above Mo. Edge/Corner: weaker and slightly red-shifted; spacing to Nb–O–Nb shrinks.	Tet provides a localized, stiff M–O(tet) with large parallel-tensor response (A_g). Octahedral environments delocalize/mix the stretch, reducing Raman tensor amplitude and shifting frequency.

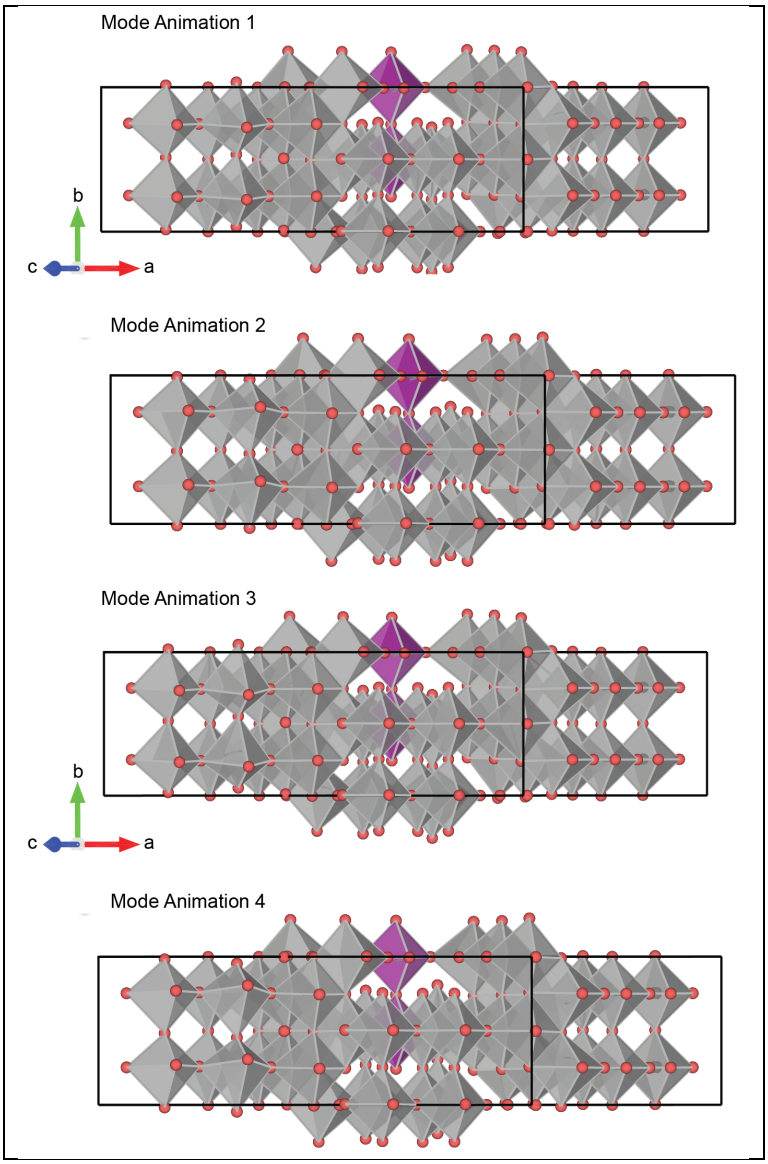
Mode Animation 1
b
c
a
Mode Animation 2
Mode Animation 3
b
c
a
Mode Animation 4

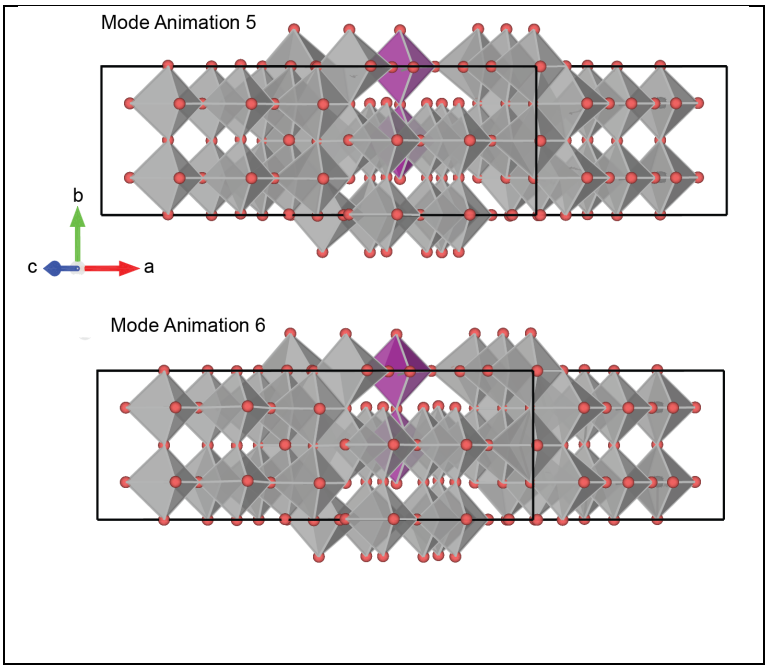

Figure S5. Raman mode animations associated with the spectral feature at 630 cm^{-1}.

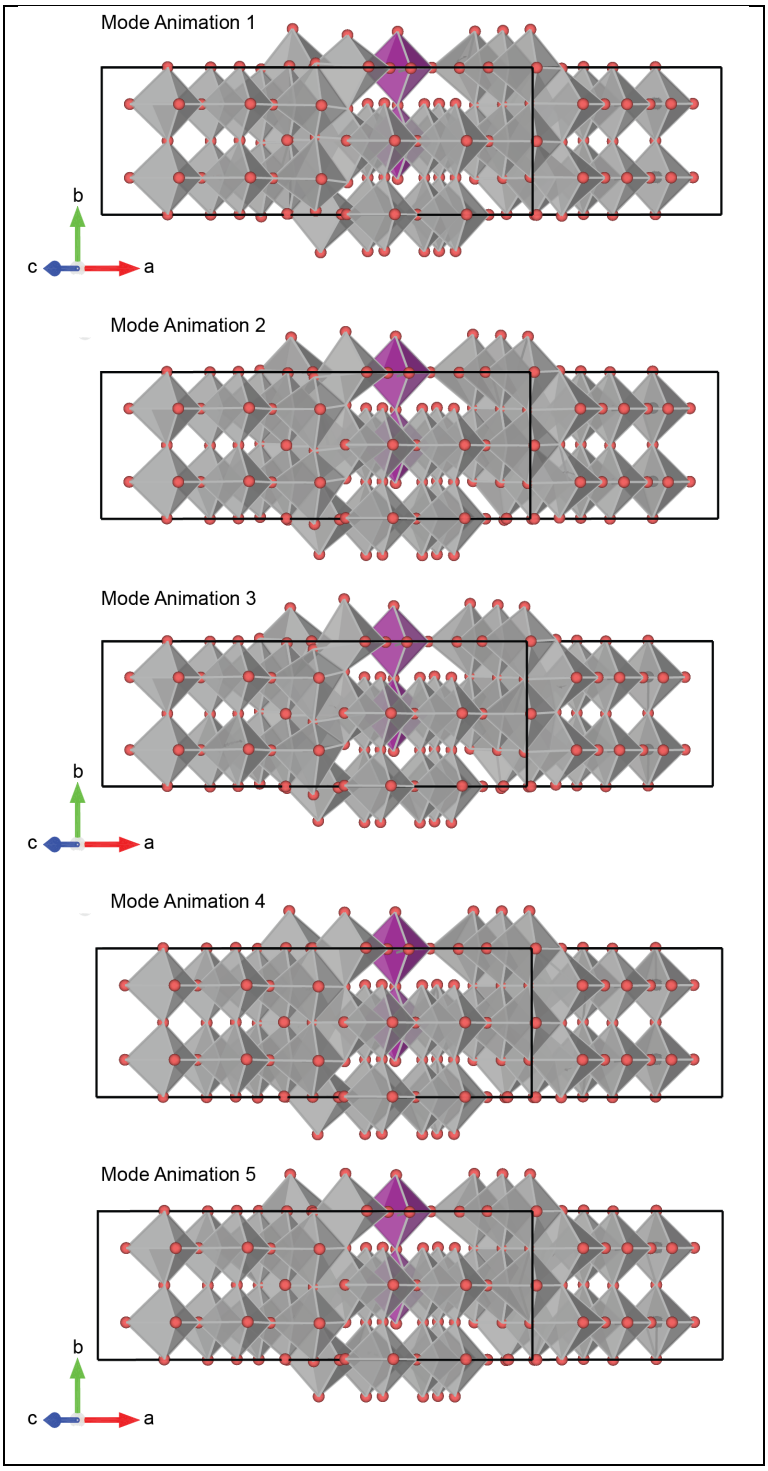

Figure S6. Raman mode animations associated with the spectral feature at 630 cm^{-1}.

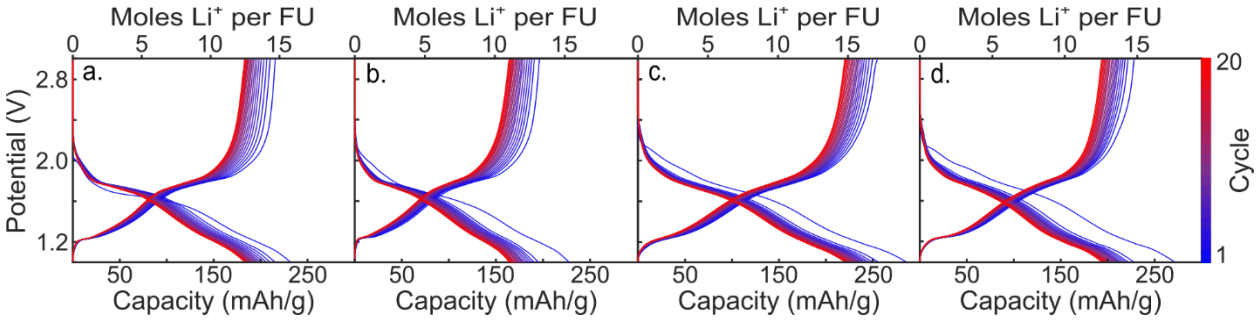

Figure S7. Charge-discharge data for (a) R-$Nb_{12}WO_{33}$, (b) R-$Mo_{.25}W_{.75}Nb_{12}O_{33}$, (c) R-$Mo_{.75}W_{.25}Nb_{12}O_{33}$, and (d) R-$MoNb_{12}O_{33}$ measured at a C/3 rate.

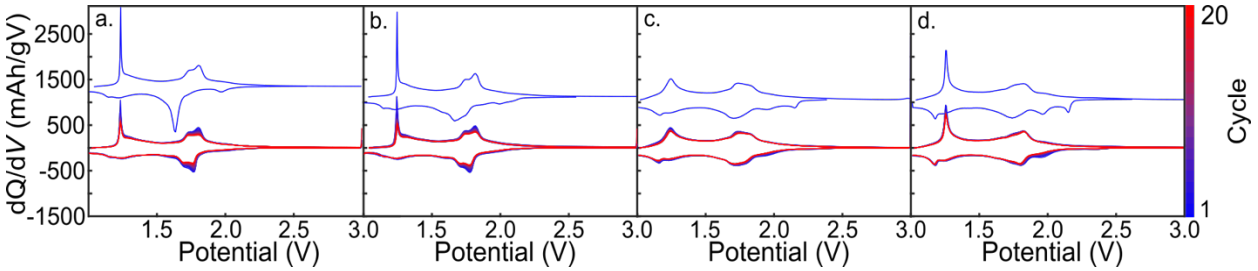

Figure S8. dQ/dV plots for (a) R-$Nb_{12}WO_{33}$, (b) R-$Mo_{0.25}W_{0.75}Nb_{12}O_{33}$, (c) R-$Mo_{0.75}W_{0.25}Nb_{12}O_{33}$, and (d) R-$MoNb_{12}O_{33}$.

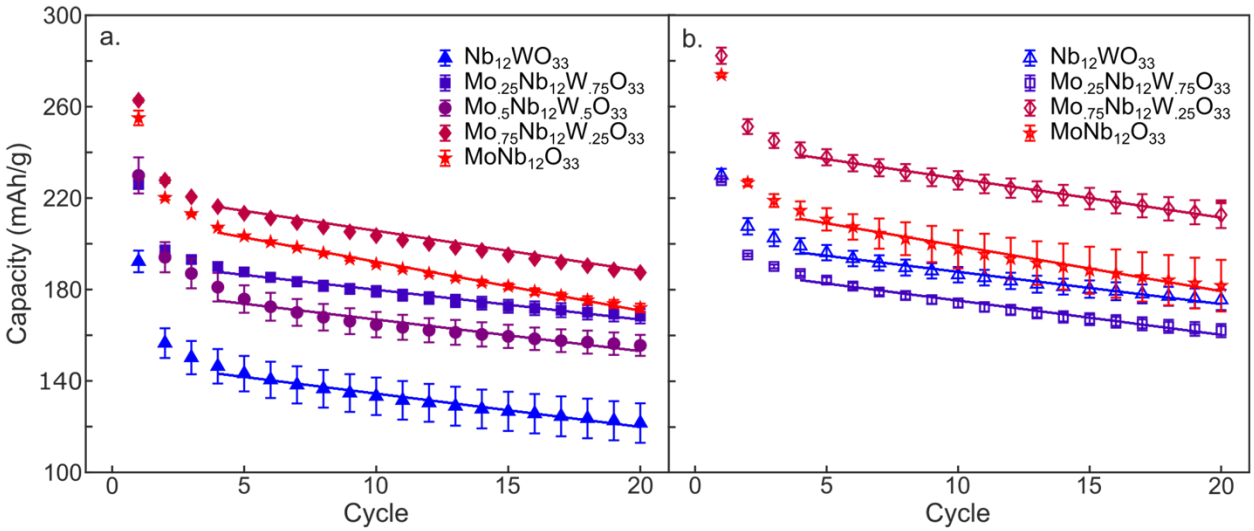

Figure S9. Average discharge capacity versus cycle number (triangles) for (a) $Mo_xW_{1-x}Nb_{12}O_{33}$ and (b) R-$Mo_xW_{1-x}Nb_{12}O_{33}$. The solid lines in panel (a) represent linear fits to the data for cycles 4-20, yielding slope values of and is –1.60, –1.38, –1.57, –1.82, and –2.24 $mAhg^{-1}$/cycle for x=0, 0.25, 0.5, 0.75 and 1, respectively. The slope values for panel (b) data are –1.40, –1.49, –1.70, and –1.98 $mAhg^{-1}$/cycle for x=0, 0.25, 0.75 and 1 respectively.

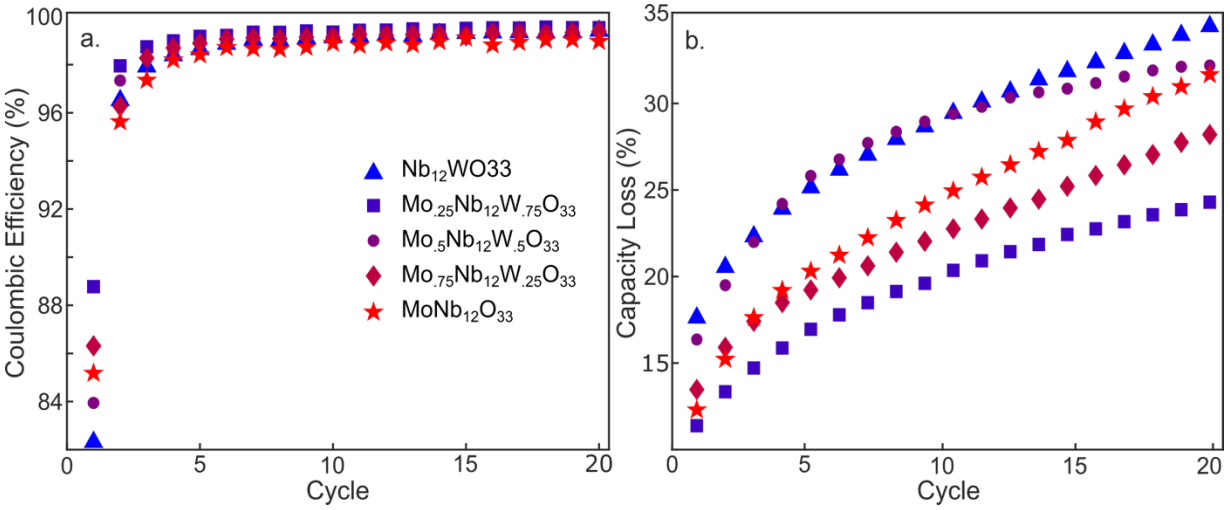

Figure S10. Average (a) coulombic efficiency of $Mo_xW_{1-x}Nb_{12}O_{33}$ and (b) percent capacity loss relative to cycle 1.

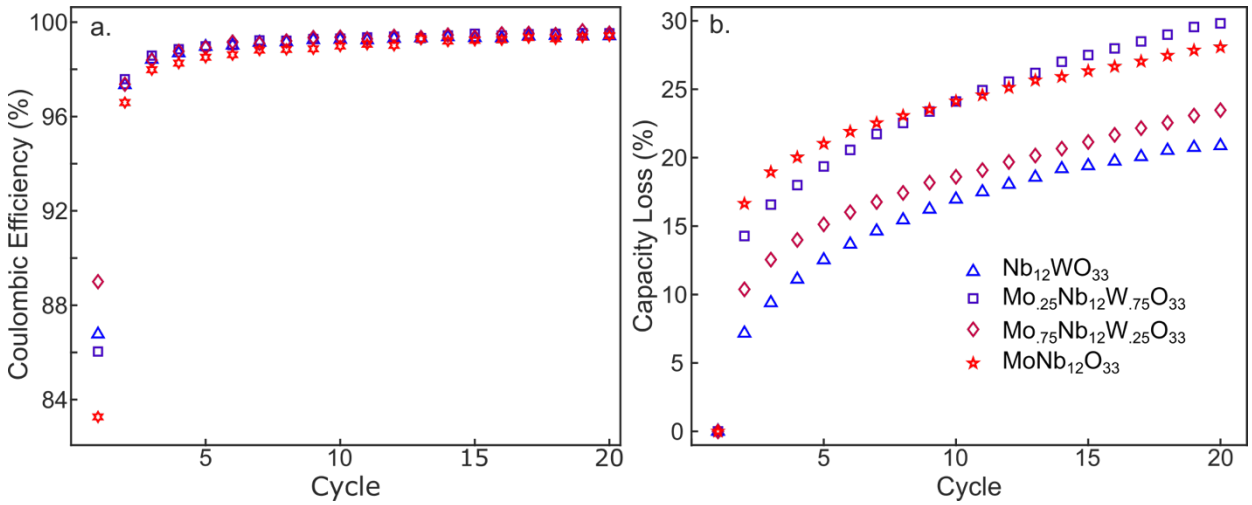

Figure S11. (a) Average coulombic efficiency for R-$Mo_xW_{1-x}Nb_{12}O_{33}$. (b) Average capacity loss relative to the first cycle for R-$Mo_xW_{1-x}Nb_{12}O_{33}$.